J. Fluid Mech. (1986), *vol.* 173, *pp.* 519–544
Printed in Great Britain

Space-laboratory and numerical simulations of thermal convection in a rotating hemispherical shell with radial gravity

By JOHN E. HART,

Department of Astrophysical, Planetary and Atmospheric Sciences, University of Colorado, Boulder, CO 80309, USA

GARY A. GLATZMAIER

Earth and Space Sciences Division, MS F665, Los Alamos National Laboratory, Los Alamos, NM 87545, USA

AND JURI TOOMRE

Joint Institute for Laboratory Astrophysics, and Department of Astrophysical, Planetary and Atmospheric Sciences, University of Colorado, Boulder, CO 80309, USA

(Received 27 March 1986)

The Sun and the giant planets rotate and possess deep shells of convection. Some basic aspects of prototypical global convection have been studied with a laboratory model operated in the microgravity environment of Spacelab 3 that flew on the space shuttle Challenger in May 1985. This experiment studied thermally driven circulations within a rotating hemispherical shell of fluid across which are imposed radial and latitudinal temperature gradients. The radial force of gravity is modelled by imposing a strong electric field across the shell, with dielectric polarization forces producing radial accelerations proportional to temperature. When the influence of rotation is large, the experiments yield north–south oriented columnar convection in equatorial and subequatorial regions. As the differential heating is increased, these roll-like cells interact with mid-latitude waves, ultimately being destroyed by turbulent, horizontally isotropic convection that moves down from the pole. When a significant equator-to-pole temperature difference is imposed on the boundaries, spiral waves develop on top of a strong meridional circulation. Intricate, non-axisymmetric, convective patterns that propagate in longitude and evolve in time are described. Schlieren visualizations of these laboratory flows are compared with three-dimensional nonlinear simulations.

1. Introduction

Large-scale atmospheric motions driven by thermal forcing on rotating planets like Earth are largely controlled by buoyancy and Coriolis forces. Circulations seen in the atmospheres of the giant outer planets like Jupiter, Saturn and Uranus, and probably extending deep within these gaseous planets, must also be dominated by these forces. A combination of buoyancy and Coriolis forces is also likely to control global-scale flows in the convection zones of rotating stars like the Sun. Certainly the motions that result are likely to be quite different, for the energy sources that drive these various forms of convection range from differential solar heating for Earth, to a mixture of insolation and gravitational contraction for the gaseous planets, and to

nuclear burning for a star. Yet a unifying feature of all these objects is that they are spherical and that they rotate, and thus the horizontal component of the Coriolis force varies with latitude. This variation is thought to be crucial in determining the differential rotation of the Sun and the structure of its giant convection cells (as reviewed, for example, by Gilman 1986), the cloud-band orientations and zonal flows on Jupiter and Saturn (e.g. Ingersol *et al.* 1980; Busse 1983), large-scale waves and the mid-latitude jet streams on Earth (e.g. Charney 1947; Charney & Drazin 1961), and the generation of magnetic fields by dynamo action in many of these objects (e.g. Moffatt 1978; Parker 1979). All of these thermally driven flows are of sufficient scale in the north–south direction that the sphericity and the resulting latitudinal variation of Coriolis force have a strong influence on the dynamics.

It has been difficult to model such spherical flows properly in the terrestrial laboratory: the rotation $\boldsymbol{\Omega}$ and gravitational acceleration $\boldsymbol{g}$ vectors must be parallel to avoid oscillatory gravity in the rotating reference frame, whereas in planets and stars $\boldsymbol{\Omega}$ and $\boldsymbol{g}$ are stationary and range from parallel at the pole to perpendicular at the equator. Thus the full latitude dependence of Coriolis forces on spherical surfaces has been hard to capture. Busse & Carrigan (1976) and Carrigan & Busse (1983) have used the centrifugal-buoyancy effect to advantage in laboratory studies of convection in spherical shells. In their model 'gravity' is everywhere nearly perpendicular to the axis of rotation. The centrifugal-buoyancy experiments have illustrated and confirmed several previously predicted properties of convection in equatorial and mid-latitude regions of very rapidly rotating objects. These properties include a preferred orientation of convection along the axis of rotation in the form of 'banana cells' (Busse 1970, 1973; Durney 1970). Our experiments show similar convective structures in the appropriate parameter ranges (i.e. high Taylor number, spherically symmetric differential heating). We have also observed several phenomena that appear to depend crucially on the varying orientation of $\boldsymbol{g}$ and $\boldsymbol{\Omega}$ as one moves from equator to pole, and which could not be studied in the centrifugal-convection apparatus where the component of gravity parallel to the axis of rotation is neglected. For example, the centrifugal-convection experiment cannot consistently address interactions of polar and equatorial convection modes, nor be used to study the evolution of the global-scale convective structures that occur at low rotation rates and which span large extents in latitude.

We have developed and tested a method for studying convection within a rotating spherical shell of fluid, using electrohydrodynamic polarization forces to generate the required *radial* buoyancy forces. In a dielectric liquid subject to imposed electric-field and thermal gradients, there will be temperature-dependent polarization forces present in addition to normal buoyancy. However, the electrostatic 'radial gravity' resulting from the polarization forces is relatively weak (typically one-tenth of the value of terrestrial gravity g), and therefore experiments that are not to be contaminated by g-effects need to be conducted in a microgravity laboratory. Our only reason for going into space with this experiment is to effectively turn off the unidirectional gravity which masks the fundamental dynamical interactions that we wish to observe. The flight of the Spacelab 3 microgravity laboratory onboard the space shuttle Challenger in May 1985 enabled us to conduct such electroconvection experiments using our instrument, the 'Geophysical Fluid Flow Cell' (or GFFC).

As described briefly in Hart *et al.* (1986) and elaborated in §2 of this paper, the GFFC experiment is a differentially heated, hemispherical shell of fluid, containing dielectric silicone oil, which is mounted on a turntable that rotates at constant specified rates. Zonally symmetric temperatures are maintained on the boundaries

by computer-controlled heaters and coolers. The thermal boundary conditions are axisymmetric, but allow for both inner- and outer-surface temperature variations with latitude. An alternating high-voltage applied between the inner and outer boundaries produces a radially directed, density-dependent electrostatic force that simulates a central gravity. Since the hemispherical shell of fluid is bounded on the outside by a transparent sapphire dome, the convective flow patterns are readily visualized by Schlieren and shadowgraph photography.

The Spacelab 3 flight permitted us to perform experiments with the GFFC for about 110 h. These generated some 50000 photographic data frames that contain images of convective structures, instabilities and turbulence, under varying conditions of differential heating and rotation. Several new types of convection were observed: mid-latitude waves interacting with the low-latitude columnar convection rolls previously studied by Carrigan & Busse (1983), 'spiral waves' near the poles when latitudinal heating gradients are present on the bounding surfaces, and 'triangular waves' coupling mid-latitude and equatorial disturbances under similar differential heating. In addition, we also observed the breakdown of the banana cells as the combination of electrodynamic gravity and differential heating that serves to drive the convection is increased.

Our goals are to elucidate, with a combination of laboratory experiment and numerical computation, some of the more fundamental aspects of convection in simple spherical cavities of relevance to both planetary and stellar dynamics. For instance, how does convection redistribute angular momentum within shells of fluid which are unstably stratified, does the resulting differential rotation have varying forms depending upon the magnitude of imposed latitudinal gradients in temperature, and what are the cell shapes and wavy disturbances of global-scale convection as the rotational constraint and the differential heating are varied to span both high and low rotation rates, and both spherically symmetric and latitudinally varying differential heating?

In §2 we begin by discussing some basic principles of electrohydrodynamics, showing how these led to the design of the GFFC instrument and its manner of operation. The reduced equations and boundary conditions are also presented. In §3 we show some of the experimental results from the flight of the instrument on Spacelab 3, briefly illustrating the variety of convection achieved by varying the imposed radial and latitudinal temperature gradients, rotation rates and the strength of the electrostatic gravity. In §4 we compare the results with those obtained from our nonlinear three-dimensional simulations of such convection, finding general agreement at the more modest parameter values that are accessible using present-day supercomputers. In §5 we summarize what we have found so far from our analysis of these experiments carried out in the microgravity laboratory.

2. Description of the experiment

We first show how electrodynamic polarization forces in a dielectric liquid can be used to enable the study of thermal convection in a spherical shell with radial gravity. Certain constraints on the experimental parameter ranges, due to the physical properties of available fluids that are safe enough to be used on manned spaceflights, will be discussed. The basic idea of using dielectrophoretic effects to model flows with central buoyancy forces was apparently first suggested by Smylie (1966) who gives a preliminary description of a model of convection between two cylinders, across which both differential temperatures and voltages are applied. We were unaware of

this paper when we initiated our design in 1971. The experimental study of rotating flows in spherical geometry that are of interest to geophysicists and astrophysicists presents more of a technical than a conceptual challenge. A central issue is the visualization of spatial structures in convecting fluids that are so highly stressed (electrically) that the insertion of probes or particles is impossible. This section describes the basic principles of the experiment, the techniques used for monitoring the motions and controlling the boundary conditions, and the interface with the astronaut operators.

2.1. *Electrohydrodynamics*

The basic Boussinesq equations of motion for a rotating dielectric liquid are

$$\frac{\partial \boldsymbol{v}}{\partial t}+(\boldsymbol{v}\cdot\boldsymbol{\nabla})\,\boldsymbol{v}+2\boldsymbol{\Omega}\times\boldsymbol{v}=-\frac{1}{\bar{\rho}}\,\boldsymbol{\nabla}p+\nu\nabla^2\boldsymbol{v}+g\alpha T\hat{\boldsymbol{r}}-\alpha T\Omega^2 r_\perp+\frac{\boldsymbol{F}}{\bar{\rho}}, \tag{1}$$

$$\boldsymbol{\nabla}\cdot\boldsymbol{v}=0, \tag{2}$$

$$\boldsymbol{F}=q\boldsymbol{E}-\tfrac{1}{2}E^2\boldsymbol{\nabla}\epsilon+\tfrac{1}{2}\boldsymbol{\nabla}\left(E^2\rho\,\frac{\mathrm{D}\epsilon}{\mathrm{D}\rho}\right), \tag{3}$$

$$\boldsymbol{\nabla}\cdot\epsilon\boldsymbol{E}=\epsilon\boldsymbol{\nabla}\cdot\boldsymbol{E}+\boldsymbol{\nabla}\epsilon\cdot\boldsymbol{E}=q,\quad \boldsymbol{\nabla}\times\boldsymbol{E}=0, \tag{4a,b}$$

$$\frac{\partial q}{\partial t}+(\boldsymbol{v}\cdot\boldsymbol{\nabla})\,q=-\boldsymbol{\nabla}\cdot\boldsymbol{J}, \tag{5}$$

$$\frac{\partial T}{\partial t}+(\boldsymbol{v}\cdot\boldsymbol{\nabla})\,T-\kappa\nabla^2 T=\Phi+\frac{\partial\epsilon}{\partial T}\,T\,\frac{\mathrm{D}E^2}{\mathrm{D}t}\Big/2\bar{\rho}c, \tag{6}$$

where $\boldsymbol{v}$ is the velocity, p the pressure, ρ the density, ν the kinematic viscosity, $\boldsymbol{\Omega}$ the basic rotation rate, g the gravitational acceleration (unidirectional in the terrestrial laboratory, fluctuating in the orbiting vehicle), α the thermal expansion coefficient, $r_\perp$ the perpendicular distance from the axis of rotation, and $\boldsymbol{F}$ the vector body force due to electrical effects. In (3)–(5) ϵ is the dielectric permittivity, q the free-charge density, $\boldsymbol{E}$ the electric field, and $\boldsymbol{J}$ the electric current. In the energy equation (6), T is the temperature, κ the thermal diffusivity, Φ the dissipative heating (containing both the kinetic and electric parts), and c is the specific heat. Equations (3)–(5) are discussed in standard textbooks (e.g. Panofsky & Phillips 1955; Stratton 1941), and (6) is familiar except for the term depending on $\boldsymbol{E}$ that represents the work done by the electric forces (Finlayson 1970). Of all the electric effects usually present in this latter equation, this work term, along with the dissipative heating contained in Φ, will represent the dominant electrodynamic effects.

The equations written above are supplemented by the equations of state that are taken to be

$$\rho=\bar{\rho}(1-\alpha T), \tag{7}$$

$$\epsilon=\bar{\epsilon}(1-\gamma T), \tag{8}$$

$$\boldsymbol{J}=\sigma\boldsymbol{E}, \tag{9}$$

where γ is the change of ϵ with temperature, $\bar{\epsilon}$ the ambient permittivity (constant), $\bar{\rho}$ the ambient density (constant), and σ the electrical conductivity of the fluid.

There are many classes of electrohydrodynamic motions that are described by these equations and associated boundary conditions. These are reduced somewhat if impermeable and infinitely conducting boundaries (both electrically and thermally) are imposed, since then the electrohydrodynamic and surface-tension induced

instabilities that occur when free surfaces are present (as described, for example, by Melcher & Taylor 1969 and Ostrach 1982 respectively), and which do not have obvious large-scale geophysical analogues, are suppressed. We next observe that because the fluid is incompressible, no flows will be induced by the last term in (3) which represents electrostriction and contributes only to a modified pressure. There is still a large group of motions that can be attributed to, or modified by, charge transport in the fluid. The charge transport can be affected by thermally induced changes in the conductivity leading to electroconvection, even in stably stratified fluids (Roberts 1969; Turnbull 1971; Worraker & Richardson 1981). Instabilities related to charge separation can also occur in an isothermal weakly conducting fluid (Atten & LaCroix 1979, and references therein, give both theoretical and experimental evidence). Since we are interested in buoyant, or thermally induced motions, it is necessary to eliminate the first term in (3). This is done by considering flows only in an alternating electric field where the frequency of oscillation ω is chosen to be very large with respect to the charge relaxation frequency, or, using the data in table 1,

$$\omega \gg \frac{\sigma}{\bar{\epsilon}} \approx 0.2 \text{ s}^{-1}. \tag{10}$$

That the remaining force term in (3) leads to electrodynamic buoyancy is easily seen by combining this term with the state equations (7)–(8), and removing all contributions that can be subsequently written as the gradients of a scalar 'modified pressure'. The only remaining bulk force per unit mass that contributes to vorticity generation in the fluid is thus

$$\boldsymbol{F}_{\text{em}} = -\frac{\bar{\epsilon}\gamma T}{2\bar{\rho}} \nabla(\boldsymbol{E}\cdot\boldsymbol{E}). \tag{11}$$

It is therefore seen that $\boldsymbol{E}\cdot\boldsymbol{E}$ acts like a geopotential, and that γ plays the role of the thermal expansivity in the usual Boussinesq buoyancy term. The electric field $\boldsymbol{E}$ is found by solving (4) with $q = 0$. Note that because ϵ varies, $\boldsymbol{E}$ will not in general be radial or uniform, even between parallel plates at constant potentials V_1 and V_2, say. This latter case was studied by Turnbull & Melcher (1969), who showed that gradients of E^2 generated by variations in $\epsilon(T)$ could lead to thermally coupled electroconvection. If the boundary shapes are such that ∇E^2 is strongly non-zero even under isothermal conditions, effects due to variations of ϵ with T in (3) will be of minor importance. Thus we make the assumption, equivalent to that usually made for a Boussinesq liquid, that ϵ is assumed constant except where multiplied by the electrostatic 'gravity', $\bar{\epsilon}\nabla E^2/2\bar{\rho}$. The Clausius–Mossoti relation

$$\frac{\gamma}{\alpha} = \frac{(\bar{\epsilon}-\epsilon_0)(\bar{\epsilon}+2\epsilon_0)}{3\epsilon_0\bar{\epsilon}}, \tag{12}$$

where ϵ_0 is the vacuum permittivity, shows that for our working fluid γ is only slightly smaller than the thermal expansion coefficient α, so this is a good assumption when ∇E^2 is forced to be large.

2.2. *Design considerations*

Figure 1 shows a schematic of our experiment. The inner boundary is a nickel-plated steel sphere. The outer shell is made up of a transparent sapphire hemispherical dome with a transparent Indium-oxide electrically conducting coating applied to its inner surface. It is connected at the equator to a lower hemispherical dome made out of aluminium. The radii of the inner and outer surfaces are R_1 and R_0 respectively. A 300 Hz a.c. voltage V is applied across the dielectric working fluid, a low-viscosity

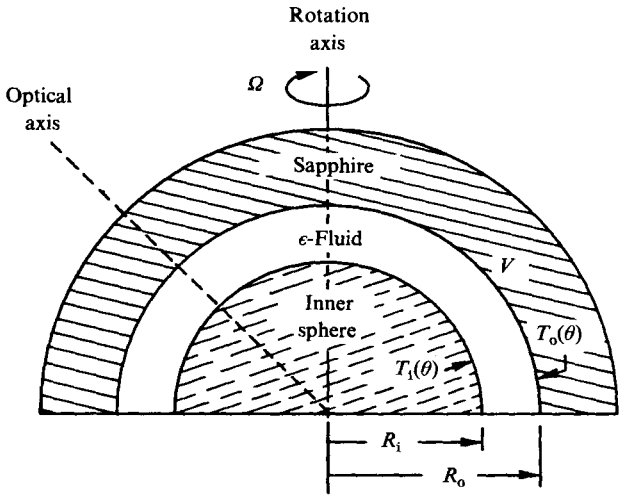

FIGURE 1. Cross-section of the test cell used to study global convection in a rotating hemispherical shell of fluid in the presence of an electrostatic radial gravity field. That gravity is achieved by imposing an alternating potential V across the fluid shell. The dielectric silicone working fluid is bounded on the outside by a transparent sapphire dome to allow optical probing of the flows and thermal structures that accompany the convection driven by differential heating.

Nominal Fluid Properties (Dow Corning 0.65 cs 200 Fluid)		
Ambient density	$\bar{\rho}$	760 kg/m^3
Expansivity	α	1.34×10^{-3} °C^{-1}
Kinematic viscosity	ν	6.5×10^{-7} m^2/s
Thermal diffusivity	κ	7.7×10^{-8} m^2/s
Ambient permittivity	$\bar{\epsilon}$	$2.5\epsilon_0$
Vacuum permittivity	ϵ_0	8.90×10^{-12} farad/m
Dielectric variability	γ	1.29×10^{-3} °C^{-1}
Conductivity	σ	10^{-12} mho/m
Heat capacity	c	1.7×10^3 joules/kg °C
Dissipation loss factor	ϕ	$\approx 4 \times 10^{-5}$
Nominal Experiment Parameters		
Rotation rate	Ω	0–3 rad/s
Radial temp. difference	ΔT_r	0–25 °C
Voltage (r.m.s.)	V	0–10 kV
Voltage frequency	ω	300 Hz
Inner radius	R_i	2.402 cm
Outer radius	R_o	3.300 cm
Gap	d	0.908 cm
Aspect ratio	$\beta = R_i/d$	2.65
Prandtl number	Pr	8.4

TABLE 1

silicone oil whose nominal properties are listed in table 1. The experiment is conducted in the upper hemisphere; a teflon baffle fills the annular space below the equator down to a narrow neck that carries thermal and electrical lines to the inner sphere (not shown in figure 1, but an exterior view can be seen in figure 2). Because of this narrow feedthrough at the south pole, the device is not a true spherical capacitor, and fringing

fields with non-spherically symmetric potentials will exist. However at and above the equator, $\boldsymbol{E}$ varies essentially as $r^{-3}\boldsymbol{r}$. In the working fluid the electrodynamic buoyancy force can thus finally be written as

$$\boldsymbol{F}_{\rm em} = g_0 \gamma T \hat{\boldsymbol{r}}, \tag{13}$$

with an effective electrostatic gravity

$$g_0 = \frac{2\bar{\epsilon} V_{\rm rms}^2 \beta^2 R_{\rm o}^5}{(1+\beta)^3 d^3 \bar{\rho} r^5}, \tag{14}$$

where d is the gap width $R_{\rm o} - R_{\rm i}$, and β is the geometric aspect ratio $R_{\rm i}/d$. The 'gravity' falls off like r^{-5}, instead of like r^{-2} as one might like for geophysical modelling. This problem has been addressed by Hart & Toomre (1977) who studied the linear instability problem in spherical shells with varying gravity distributions. For the aspect ratio of the experiment, the linear eigenfunctions are almost identical (see also Markiewicz & Aldridge 1982), suggesting that the qualitative structure of the observed convective motions would be expected to persist in the presence of an inverse-square-law gravity.

Several compromises in the design of the spherical convection experiment now become evident. One would like a large value of d and $R_{\rm i}$ so that nearly inviscid and rapidly rotating flows [i.e. high Taylor and Rayleigh numbers, as defined below in (18) and (19)] can be studied. However as $R_{\rm i}$ and d increase the electrostatic gravity falls rapidly. In addition, an essentially radial buoyancy force is only attained if the centrifugal acceleration $\Omega^2 r_\perp$ is small compared with g_0. This constraint also leads to small spheres and moderate rotation rates. In the end, the specifications in table 1 were chosen to enable the study of a large range of slowly and rapidly rotating convection problems with Taylor numbers from 0 to 6×10^5 and Rayleigh numbers (based on g_0 at the outer sphere) from 0 to over 10^6. The latter value is well over one hundred times critical at Taylor numbers less than about 10^6.

When the parameters are chosen to optimize the experimental parameter-space range, it quickly becomes obvious, upon comparing g_0 with g, that unless a liquid with a very large value of $\bar{\epsilon}$ is used, terrestrial gravity will swamp out the weak (less than 1 m/s^2) electrostatic radial acceleration. Unfortunately such fluids tend to be polar with low dielectric strengths, have large viscosities, and are usually highly toxic.

2.3. *Reduced equations and boundary conditions*

With the assumptions outlined above we can write the non-dimensional equations of motion using scales d for position, d^2/κ for time, κ/d for velocity, ΔT_r (the imposed radial boundary temperature difference) for temperature, and $\kappa^2\bar{\rho}/d^2$ for pressure. The flow relative to the static field that ensues when the boundary temperatures are uniform on spherical surfaces, and within a coordinate system rotating at the rate Ω, is thus governed by

$$\nabla \cdot \boldsymbol{v} = 0, \tag{15}$$

$$\frac{\partial \boldsymbol{v}}{\partial t} = -\nabla p + Ra\, Pr \left(\frac{1+\beta}{r}\right)^5 T\hat{\boldsymbol{r}} + Ta^{\frac{1}{2}} Pr\, \boldsymbol{v} \times \hat{\boldsymbol{\Omega}} + Pr\, \nabla^2 \boldsymbol{v} + \boldsymbol{v} \times (\nabla \times \boldsymbol{v}) - \tfrac{1}{2}\nabla v^2, \tag{16}$$

$$\frac{\partial T}{\partial t} = \nabla^2 T + \frac{\beta(\beta+1)}{r^2} v_r - \boldsymbol{v} \cdot \nabla T. \tag{17}$$

The thermal equation has been reduced by ignoring the electrical and viscous dissipation terms, which are always small compared with conduction. The unidirec-

tional gravity has been suppressed, and only the electrostatic gravity is retained. The non-dimensional numbers in the above equations are

the Rayleigh number $$Ra = \frac{\gamma \Delta T_r g_0 d^3}{\kappa \nu}, \tag{18}$$

the Taylor number $$Ta = \left(\frac{2\Omega d^2}{\nu}\right)^2, \tag{19}$$

the Prandtl number $$Pr = \frac{\nu}{\kappa}, \tag{20}$$

and the aspect ratio $$\beta = \frac{R_i}{R_o - R_i}. \tag{21}$$

These are the equations used in our numerical modelling effort described in §4. They are equivalent to those usually used in geophysical fluid dynamics to study global convection when compressibility, chemical, radiative and latent-heat effects are ignored. Although such processes can be important in natural flows, there are many fundamental issues to be resolved in systems where they are absent. The studies of Chandra & Smylie (1972) and Hart (1976) concluded that solutions of these equations are in agreement with terrestrial experiments on convective instabilities in a cylindrical annulus, and on Hadley flows in a differentially heated non-rotating spherical shell respectively.

The boundary conditions are that $\boldsymbol{v}$ vanishes on all walls of the hemispherical annulus (i.e. at $r = \beta$ and $r = 1+\beta$ for all latitudes $\theta > 0$, and at the equatorial barrier at $\theta = 0$). Latitudinally varying temperatures $T_i(\theta)$ and $T_o(\theta)$ are specified on the inner and outer spherical surfaces respectively. For all the experiments reported here, only convectively unstable cases with $T_i > T_o$ everywhere are considered. We generally wish to investigate combined radial and latitudinal differential heating. The various cases to be considered can be distinguished by the dimensionless heating parameter

$$H = \frac{\Delta T_\theta}{\Delta T_r}, \tag{22}$$

the ratio between the pole-to-equator temperature difference present along both boundaries (positive for a hotter pole) to the average radial difference. In our experiments H is either zero (spherically symmetric heating) or positive (with relatively warmer inner and outer poles). This latter preference was required by the design of the instrument's optics. A polar cooler would obscure the visualizations. In addition, it was thought, in view of the observed heat balance for Jupiter (Ingersol 1976), that such hot inner-pole objects might be of interest in the study of Jovian dynamics.

2.4. *The GFFC instrument*

Figure 2 (Plate 1) shows the sphere assembly mounted on a rotating turntable. The turntable supports the high-voltage supply as well as several thermoelectric heaters and coolers along with associated pumps and circuitry to control the latitudinal temperature distributions $T_i(\theta)$ and $T_o(\theta)$ on the bounding surfaces of the working fluid. These boundary gradients are maintained by individual heater elements embedded just 'below' the surfaces, and permit the simulation of large-scale flows with latitudinal heating differentials as mentioned above. One can see a thermistor chain running down the right-hand side of the sphere that provides information to a servo controller which regulates the imposed temperatures. Similar sets of detectors are just below the metal surface of the inner sphere.

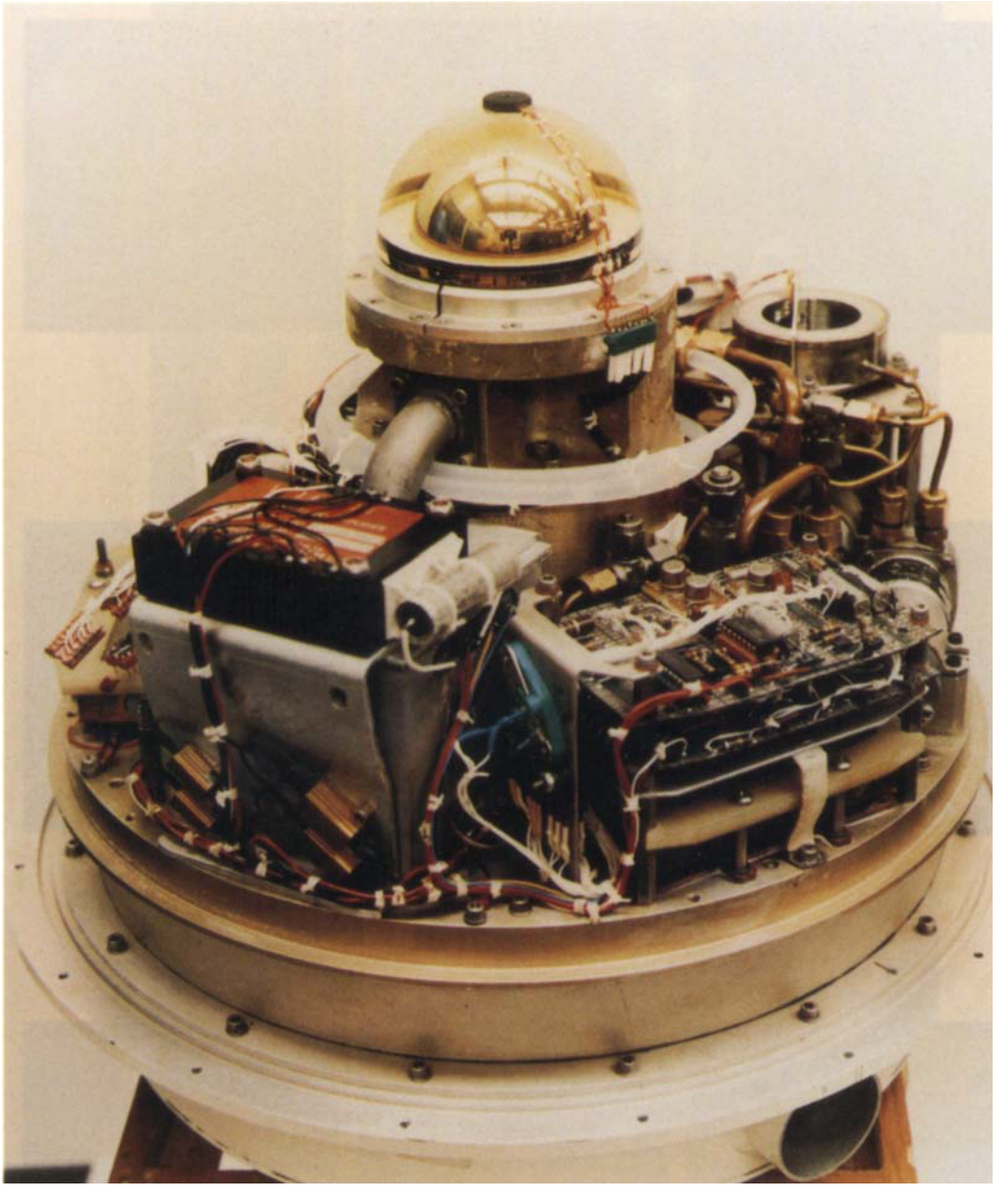

FIGURE 2. The rotating turntable supporting the high-voltage power supply (left front), the circulation pumps (right rear), the fluid cell (top), and associated circuitry that controls the temperature distributions on the boundaries of the spherical annulus. The diameter of the sphere assembly is about 9 cm.

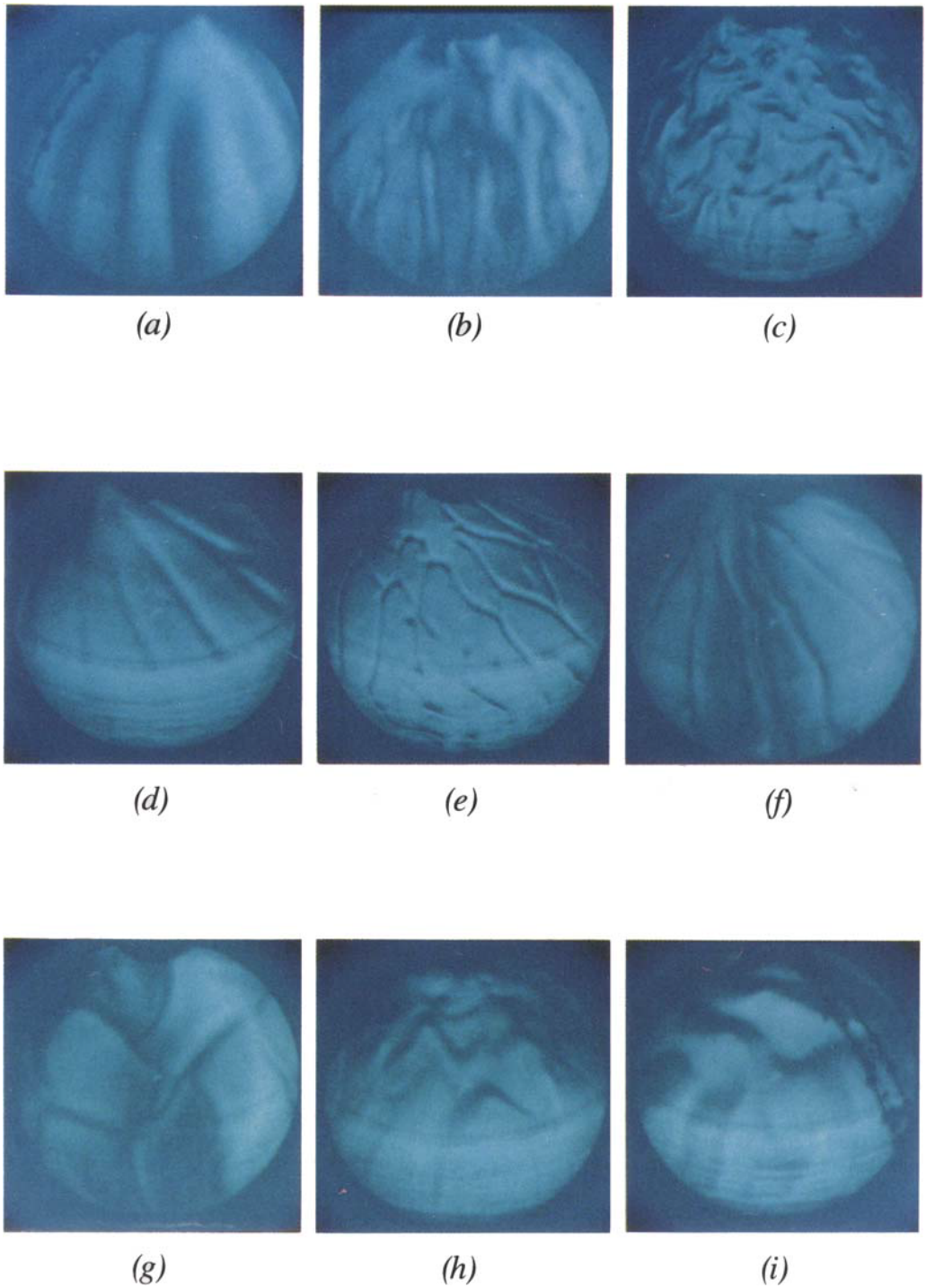

FIGURE 5. Original images from the 16 mm data film showing various forms of convection under the following conditions. *(a)* $Ra = 4.70 \times 10^3$, $Ta = 3.95 \times 10^4$, $H = 0$. *(b)* $Ra = 7.59 \times 10^4$, $Ta = 6.32 \times 10^5$, $H = 0$. *(c)* $Ra = 3.79 \times 10^5$, $Ta = 6.32 \times 10^5$, $H = 0$. *(d)* $Ra = 1.62 \times 10^4$, $Ta = 1.09 \times 10^3$, $H = 0.82$ *(e)* $Ra = 2.08 \times 10^5$, $Ta = 1.09 \times 10^3$, $H = 0.85$. *(f)* $Ra = 4.69 \times 10^4$, $Ta = 1.09 \times 10^3$, $H = 0.94$. *(g)* $Ra = 9.34 \times 10^3$, $Ta = 1.09 \times 10^3$, $H = 0$. *(h)* $Ra = 1.56 \times 10^5$, $Ta = 6.32 \times 10^5$, $H = 1.14$. *(i)* $Ra = 1.91 \times 10^4$, $Ta = 3.95 \times 10^4$, $H = 0.88$.

(a)

(b)

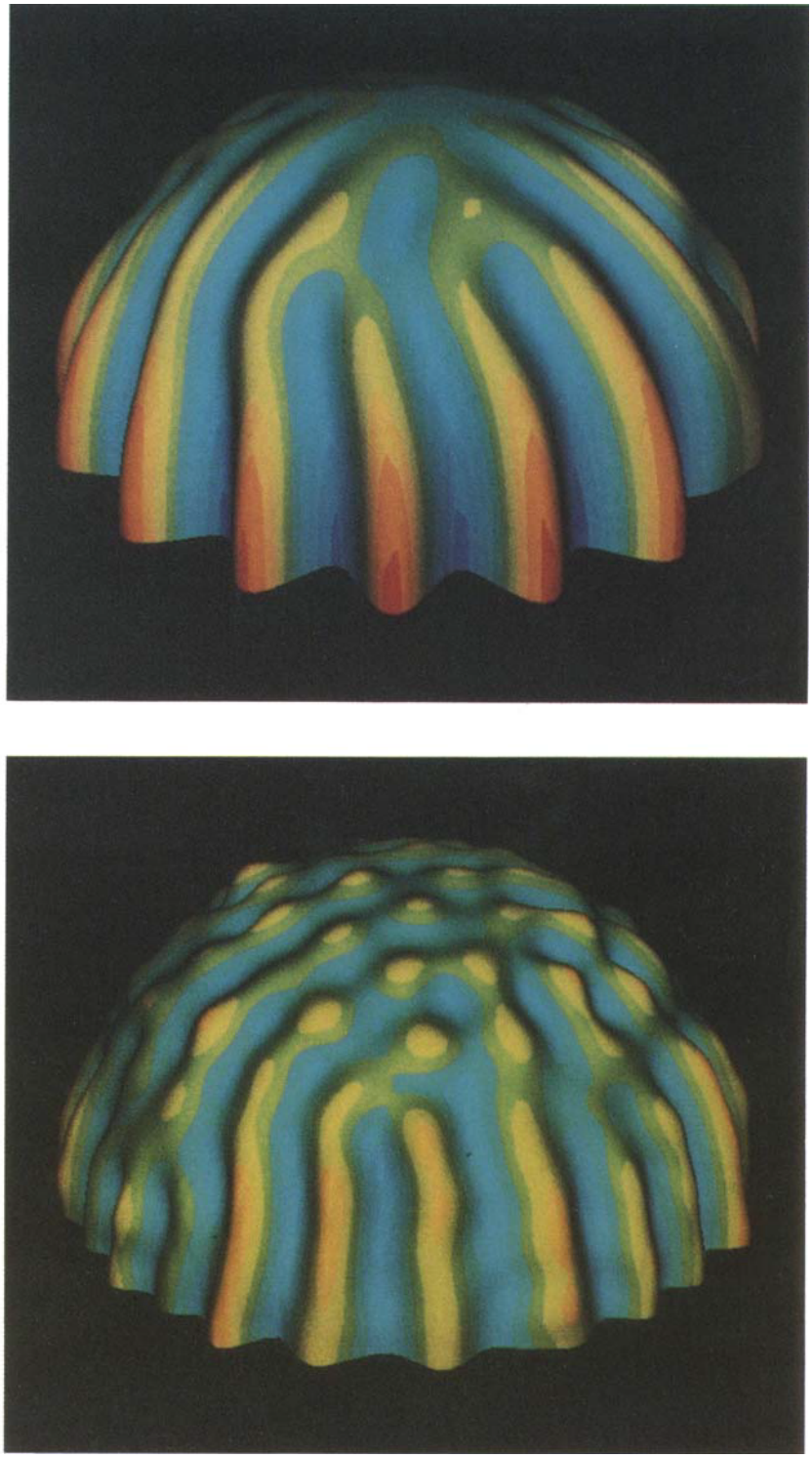

FIGURE 8. Colour perspective views from the numerical simulations at one instant in time of the radial velocity at mid-depth within the upper-hemisphere. Red = outward, blue = inward; elevation is proportional to magnitude. These simulations study the interaction of columnar convection cells aligned with the rotation axis and dominant at low latitudes with more isotropic disturbances at higher latitudes. Such convective patterns involving 'banana cells' are achieved with rapid rotation and a purely radial temperature gradient ($H = 0$). *(a)* $Ta = 3.8 \times 10^4$, $Ra = 4.1 \times 10^3$. *(b)* $Ta = 6.1 \times 10^5$, $Ra = 7.9 \times 10^4$.

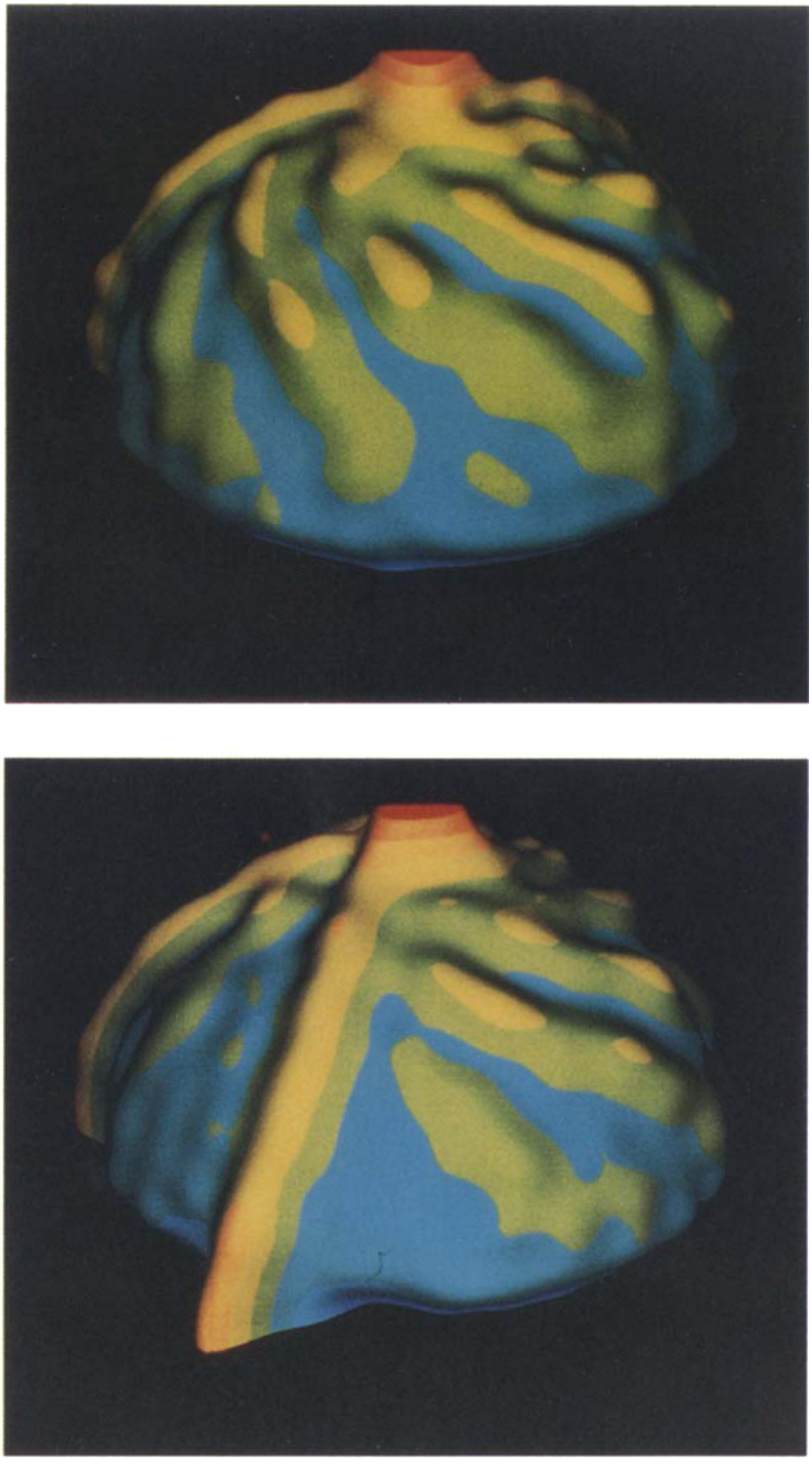

FIGURE 9. As in figure 8, but for a simulation concerned with slow rotation and combined radial and latitudinal temperature gradients, with $Ta = 1.1 \times 10^3$, $Ra = 8.4 \times 10^3$, $H = 1$. The view of the eastern hemisphere in *(a)* reveals tilted, spiral updrafts extending from the pole to mid-latitude, and these coexist in the western hemisphere *(b)* with a north–south oriented cell involving a narrow updraft extending fully from the pole to the equator.

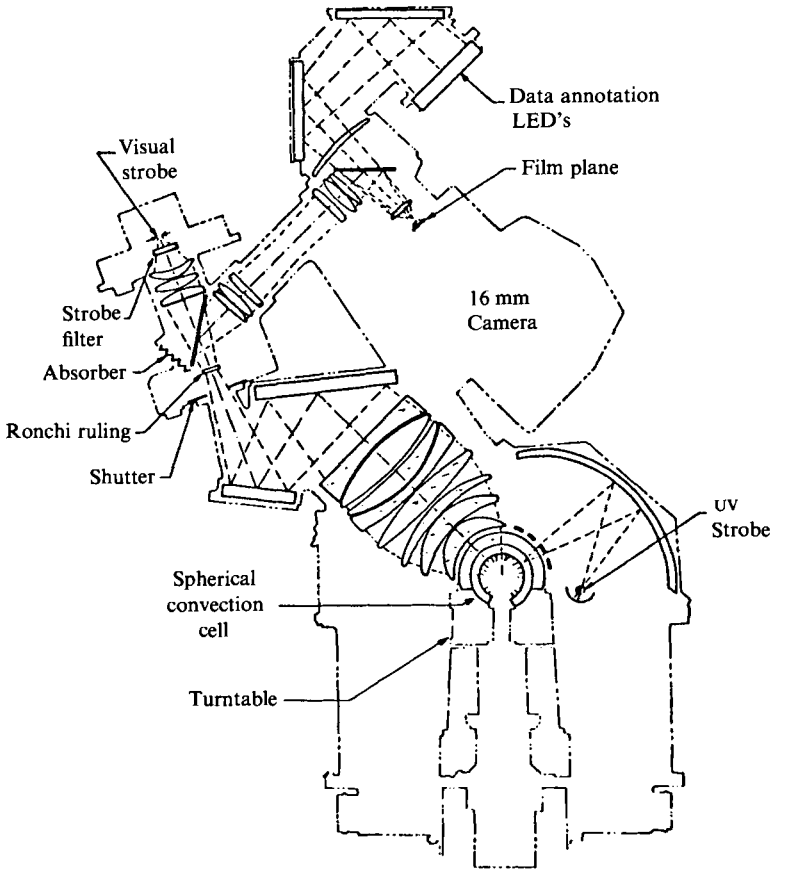

FIGURE 3. Cross-section of the optical imaging system.

Two methods of flow visualization, illustrated schematically in figure 3, are employed. A back-focus Schlieren system gives information on the radially averaged temperature structure in the convecting liquid. Light is passed through a Moiré grating of equally spaced lines and focused radially onto the inner spherical surface which is a polished mirror. The reflected rays, after being subject to refraction in the thermally perturbed liquid, are passed back through the grating and imaged onto 16 mm film. There are two orientations of the Ronchi ruling, one sensitive to roughly east–west thermal gradients and the other to essentially north–south variations. Thus, in principle, two images can be combined to yield the temperature field. In practice, pictures can only be taken sequentially with alternate gratings, and at intervals 45° or greater in longitude with 2 s or more of elapsed time between frames. At high Rayleigh numbers there is sufficient temporal variation in the flow that successive images do not reveal data on the same pattern. However the Schlieren system does not perturb the flow, and does provide global information on the convective structure.

It was intended that velocity data be obtained by using a photochromic dye called Spiro-Pyrane. This material darkens after stimulation by a collimated UV strobe, and subsequent 16 mm frames were shot to record the deformation of the dye. Unfortunately the dye degrades with time, and after the instrument was inaccessible for more than a year and a half while being integrated into Spacelab 3, it was found that at flighttime the dye contrast levels were too low to be of much use.

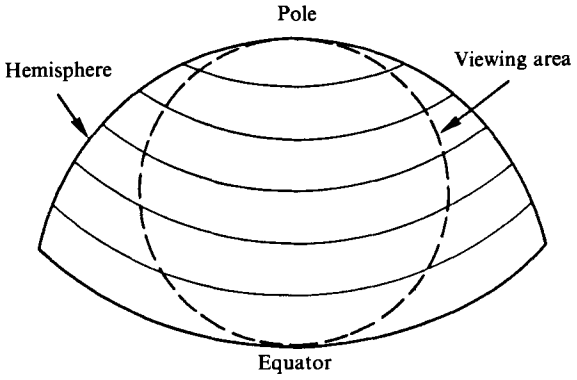

FIGURE 4. The view of the working fluid, mapped onto the sphere.

Both the dye and Schlieren data were imaged through the same wraparound optics system as shown in figure 3. The aspheric lenses provide coverage of a circular area mapped onto the hemisphere from equator to pole approximately as sketched in figure 4. Photographs were taken as the turntable rotated under the stationary optics assembly, at each 45° of longitude. Thus when the flows are weakly time dependent it is possible to reconstruct a full view of the hemisphere by combining 8 successive frames.

In the early days of this project it was not obvious that a wholly interactive terrestrial-style experiment, with continuous television downlink, was feasible. As it turned out there were long periods during each orbit with loss of signal from the shuttle. In addition astronaut time had to be shared with many experiments, and with limited resources available for interface development, it was decided to make the instrument reasonably self-contained. Thus, experiments were pre-programmed into a microprocessor that set up various rotation rates, voltages and temperatures, and then commanded the cine camera to take sequences of pictures. Light-emitting diodes (at the top-right of figure 3) that display information on the thermal and mechanical conditions of the experiment were also imaged onto each data frame. The astronauts initiated each 3 or 6 h experiment. The external conditions were set and photographs were taken over the entire duration of the run. Typically each case involved fixing the rotation rate and the heating, and then changing the applied voltage (or 'gravity') in small steps each hour. Apart from initiating experiment scenarios, and monitoring and reporting the status of the instrument, the astronauts (and the scientists on the ground) could not observe anything about the motions, and had to wait for the return of the shuttle and the processing of the data films. The interactive style of doing experiments, that will become more easily implemented in the future, would surely have been advantageous in studying secondary instabilities and transitions between various forms of convection. In spite of this drawback, a surprisingly rich collection of observations were made in the 110 h of experiments run on Spacelab 3. A synopsis of the more interesting results is contained in the next section.

3. Experimental results

3.1. *Banana cells*

Figure 5 (Plate 2) shows raw data from several of the experiments. Recall that the camera sees a circular view of the hemisphere as shown in figure 4 with the equator at the bottom and with the pole at the top. The sense of rotation in this figure, and in all other figures presented in this paper, is from right to left, so that east (prograde) is on the *left*. Figure 5(*a–c*) shows the evolution of the convective patterns at a high rotation rate as the Rayleigh number Ra is increased (by raising the voltage). These are Schlieren pictures sensitive to roughly east–west gradients. The first non-axisymmetric motions observed in this class of experiment, with moderate to high Taylor numbers and $H = 0$, always consist of slowly propagating columnar disturbances. The north–south symmetry in these modes is a consequence of the Taylor–Proudman theorem (Proudman 1916; Taylor 1921) which applies under these conditions if the differential heating is not too large. They extend from the equator to somewhat north of the so-called critical latitude, defined as the latitude where a vertical line tangent to the inner sphere hits the outer boundary. Busse & Cuong (1977) argue that when a fluid column (parallel to the axis of rotation) moves away from the axis, the spherical boundaries force it to converge if it is outside a distance from the axis equal to the inner radius, i.e. outside the tangent cylinder. As a result, regions of vorticity parallel or anti-parallel to the axis are enhanced on their prograde sides and diminished on the retrograde sides. Consequently, the convective pattern should propagate in a prograde direction. On the other hand, a fluid column inside the tangent cylinder diverges as it moves away from the axis; so patterns at high latitude should propagate in a retrograde direction. The critical latitude here is 43°, and indeed it appears that the direction of propagation switches sign in the vicinity of this latitude in agreement with these ideas. Because the columns bend in conformity with the spherical boundaries, they are often called banana cells. Such banana-cell patterns have been suggested by earlier calculations (Busse 1970, 1973; Durney 1970; Gilman 1975; Glatzmaier & Gilman 1981), and in previous multimode numerical simulations (Gilman 1977; Glatzmaier 1983).

In figure 5(*a*) the convection is relatively steady except for a weak prograde phase propagation of about 0.5° per basic rotation. When the Rayleigh number is increased, a different weakly retrograde motion ensues at mid- and high-latitudes in addition to the columnar cells in the equatorial regions. The gradients are stronger and the upwelling and downwelling regions are concentrated into narrow radial jets. The interaction between these two types of motion causes the erosion of the northward tips of the columns (figure 5*b*). This becomes more prominent as Ra is increased. Ultimately at very high Ra, equatorial columns are limited to a narrow interval near the equator (figure 5*c*). The vast majority of the sphere becomes extremely turbulent with convective elements that appear to be more or less horizontally isotropic.

3.2. *Spiral waves*

Figure 5(*d–f*) shows typical convection patterns when a substantial temperature gradient (with a hot pole) is imposed on the boundaries in addition to the unstable radial gradient. Now the fundamental instability over most non-zero Taylor numbers is spiral in nature and concentrated near the poles. The convective rolls tip west as one goes towards the equator. As Ra is increased these rolls break as branches form to make time-dependent interconnections. Yet there is still an average tilt, although the motion in figure 5(*e*), for example, is chaotic. We noticed that for several periods

during the one hour run yielding the flow shown in figure 5(*d*) (and at slightly higher Rayleigh numbers as well), the spiral pattern occasionally would be broken at certain longitudes by a convective roll extending from pole to equator without any substantial tilt. These events were fairly persistent, lasting for many basic rotations. Examples are shown in figure 5(*f*).

3.3. *Soccer balls and other cases*

A slowly rotating case is illustrated in figure 5(*g*). With $H \approx 0$ and low rotation there is no preferred direction imposed on the flow. Thus the planform observed at the end of this run is a slowly evolving tiling pattern. This case is discussed further in §4. Here we note that the updrafts (hot fluid) occur in narrow cell boundaries with broad (cooler) descending regions inside the polygons. We call this a 'soccer-ball' pattern because of the narrow ascending lines that intersect in triplets, bordering regions of sinking fluid.

Figure 5(*h*) shows a peculiar pattern that results when rapid rotation is coupled with moderate radial and strong north–south heating. Equatorial columns reappear but interact with vigorous high-latitude disturbances to form persistent 'triangular-wave' intersections at mid-latitudes. These are interpreted in §4 as resulting from an interference effect.

Finally we show a last example that is equally perplexing. When the rotation is moderate and H is about unity, we typically observe both equatorial columns at low latitudes and quasi-axisymmetric bands at high latitudes. We had hoped to observe the latter near the equator, since then we might have a candidate for the Jovian cloud belts. However figure 5(*i*) shows the most axisymmetric instability that we observed, and it is in the wrong place for Jupiter. Strong meridional circulations are expected for $H \gtrsim 1$, and the data suggest that there is a multi-cell axisymmetric circulation that is unstable to convective columns near the equator, but persists, even in the face of interactions with the tips of the columns, near the pole. That the banana cells remain, even in the presence of (strong) meridional heating, is a result of rotation winning the competition with vertical shear (generated by the thermal wind) in shaping the instabilities. The banana cells are thus quite robust objects and the theory of Busse (1983) that describes zonal-band formation by nonlinear interactions of such cells (with $H = 0$) may apply when there is meridional heating as well. Our experiments did not operate in the extremely high Taylor-number range treated in that model.

3.4. *Energetics*

Figure 6 shows wavenumber spectra obtained from digitized representations of the 16 mm Schlieren pictures. Recall that there are two grating orientations, one yielding near east–west thermal gradients and the other near north–south gradients. The relative magnitudes of each give information on the degree of horizontal anisotropy in the flow. Figure 6(*a*) indicates that the thermal gradients (and the thermal variances of these data may be obtained by dividing these curves by wavenumber m^2) are anisotropic, with more energy in the east–west direction. This is the situation for the perturbed banana cells of figure 5(*b*). When the Rayleigh number is increased, the average thermal variances become more equal (figure 6*b*), reflecting the erosion of the Taylor columns.

The spectra of the east–west gradient can be converted into thermal-variance spectra. Since most of the observed flows change considerably from picture to picture, the spectra have to be taken off a Mercator unfolding of a single circular image, although several such spectra can be averaged. This works best at mid-latitudes

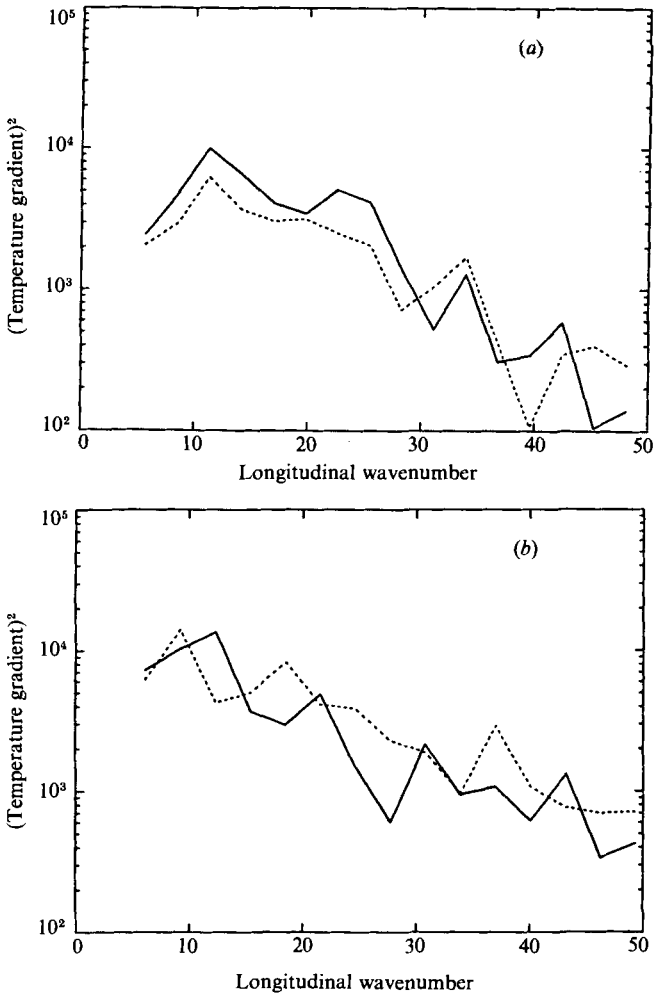

FIGURE 6. Wavenumber spectra (in arbitrary units) of the observed thermal gradients as a function of longitudinal wavenumber at latitude 50° for (*a*) as in figure 5(*b*); (*b*) as in figure 5(*c*). Solid lines reflect energy in the east–west gradients and dotted curves indicate energy in the north–south gradients.

where the longitudinal coverage and resolution in the original image is the greatest. Figure 7 shows some typical spectra that will later be compared with the results from the numerical model. They are not reliable for longitudinal wavenumbers less than about 8, since the original images cover only about 45° in longitude. It is seen that in all cases most of the thermal energy is in wavenumbers between 10 and 20, with contributions by the second and higher harmonics.

We have observed a quite varied set of convective structures. Space does not permit a detailed description of the transitions between states: discussion of these along with further analyses of the digitized data will be published elsewhere. The theoretical challenge is clearly to construct a model that at least distinguishes the pattern changes that occur when the rotation and heating parameters are varied in this experiment.

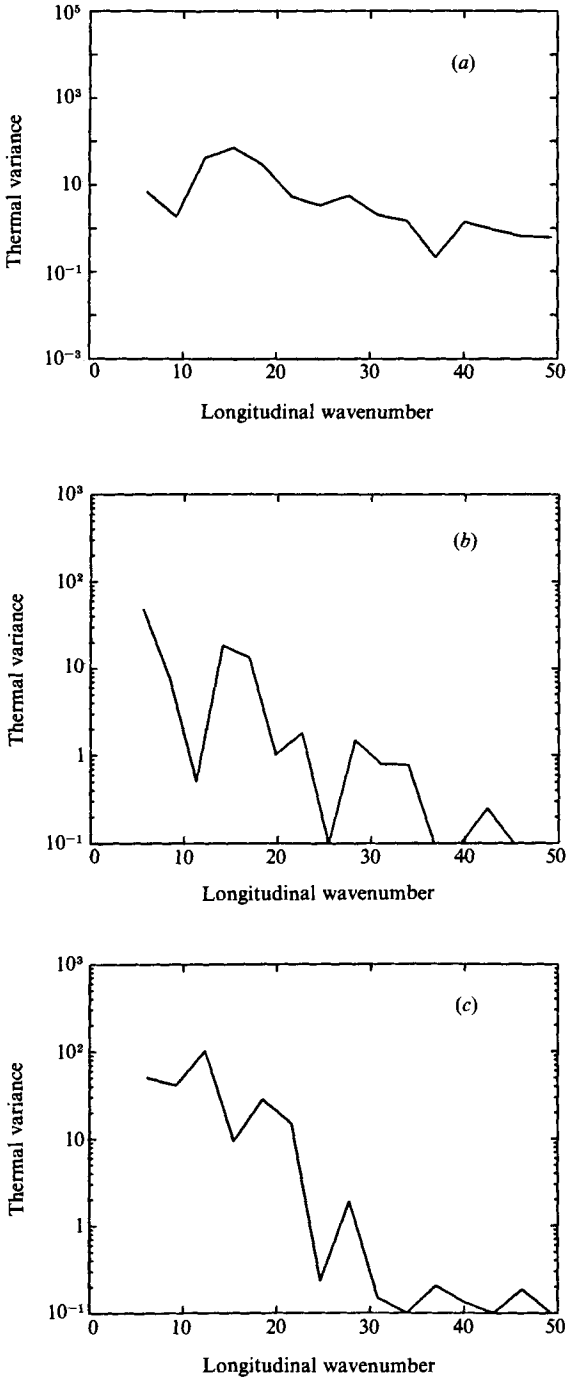

FIGURE 7. Temperature spectra for (*a*) as in figure 5(*b*) (banana cells); (*b*) as in figure 5(*d*) (spiral waves); (*c*) as in figure 5(*h*) (triangular waves).

4. Results from numerical simulations

We have chosen to augment our laboratory experiments with concurrent numerical modelling. The three-dimensional, nonlinear, Boussinesq equations (15)–(17) are solved numerically using spherical harmonics, Chebyshev expansions, and collocation in a manner similar to that outlined in Glatzmaier (1983). A sketch of our procedure is given in the Appendix. The simulations, in order, cover approximately the same Rayleigh-number cases shown in figure 5. However, constraints introduced by the need to spatially resolve the flows limits the numerical studies to $Ra \lesssim 10^5$.

4.1. *Banana cells: rapid rotation, $H = 0$*

We first discuss moderate to rapidly rotating cases for which the outer-boundary temperature and the higher inner-boundary temperature do not vary in latitude. The first case has a small Rayleigh number ($Ra = 4.1 \times 10^3$) and a moderate Taylor number ($Ta = 3.8 \times 10^4$, corresponding to an 8 s rotation period). The parameter $Ta\,Pr/Ra$ is equal to the square of the ratio of the Coriolis and buoyancy frequencies, and large values suggest a substantial influence of rotation on the convection; that ratio here is 77. A photograph of the result of this simulation is shown in figure 8(*a*) (Plate 3). The model produces convection in the form of rolls aligned with the rotation axis, and in this rendition it is clear that the name 'banana cells' is appropriate. Since radial velocity and temperature are correlated, this figure may be compared with the experimental case at essentially the same parameters (figure 5*a*). The second case has $Ra = 7.9 \times 10^4$ and $Ta = 6.1 \times 10^5$ (a 2 s rotation period). The $Ta\,Pr/Ra$ ratio is 65, a value that again suggests significant Coriolis influence. A photograph for this scenario, figure 8(*b*) (Plate 3) (see also figure 5*b*), also shows the characteristic banana-cell velocity pattern at low latitude with the axes of the convective rolls parallel to the axis of rotation. The time-averaged Nusselt number for this case is about 4.9, as defined by the ratio of heat carried through the layer when convecting to that carried by conduction alone when quiescent; the Reynolds number, $v_{\max} d/\nu$, is about 30.

In both the laboratory experiment and in the simulation, the banana-cell pattern propagates in longitude with a phase speed that is fundamentally different at high and low latitudes. As a result, the convective rolls continually shear and reconnect at mid-latitude as in figure 8(*b*). However, although the experimental and simulated convective patterns are in nice agreement, there is disagreement in the direction of the phase propagation at low latitude. In our numerical simulation the banana cells propagate in a retrograde direction with a speed substantially less than the maximum particle speed. In the experiment, the banana cells propagate at about the same speed as those in the computations, but in a prograde direction. Subsequent integrations suggest that the direction of phase propagation is sensitive to the presence of relatively weak latitudinal variations in the boundary heating. Since one of the equatorial coolers did not function on the Spacelab flight, there was a small latitudinal gradient present in all the experiments. In the presence of a latitudinal temperature gradient, certainly less than $H = 0.2$, our numerical simulations produce prograde phase propagation at low latitudes (see §4.4) in agreement with the experiment.

The kinetic energy of the computed motion is largely due to non-axisymmetric flow, and is highly time dependent. The kinetic energy of the differential rotation is only about 1 % of the total kinetic energy; and the kinetic energy of the meridional circulation is typically 0.1 % of the total. The temporal variability is illustrated in

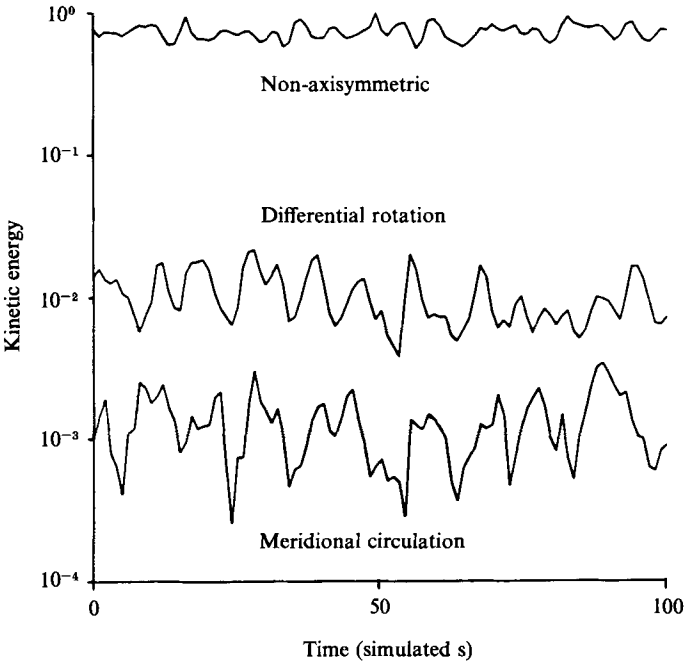

FIGURE 10. The various components of the volume-averaged kinetic energy for the solution in figure 8(*b*) with $H = 0$, $Ta = 6.1 \times 10^5$, $Ra = 7.9 \times 10^4$.

figure 10 for 100 s of simulated time (1000 timesteps). The small meridional circulation is again due to the Taylor–Proudman effect inhibiting flow parallel to the axis of rotation. As a result, the Coriolis forces that maintain the differential rotation are also small. In addition, as suggested in previous calculations (Gilman 1973, 1978), the relatively high Prandtl number and the non-slip boundary conditions tend to suppress differential rotation for high-Taylor-number cases compared to simulations with a Prandtl number of unity and stress-free boundary conditions for which the nonlinear Reynolds stress maintains differential rotation (Gilman 1977; Glatzmaier 1985). The thermal-energy spectrum (figure 14*a*) shows a peak at $m = 0$ that represents the response to zonally averaged fluxes associated with the non-axisymmetric convection. A broad secondary peak exists near $m = 16$. The kinetic-energy spectrum has a similar profile but with a minimum at $m = 0$.

4.2. *Spiral waves: slow rotation, $H \neq 0$*

The next example has an imposed equator-to-pole temperature difference on the inner and outer boundaries. The pole is hotter than the equator and the inner boundary is hotter than the outer. We consider a scenario with $Ra = 8.4 \times 10^3$, $Ta = 1.1 \times 10^3$ (48 s rotation period), and $H = 1$. Here the ratio $Ta\,Pr/Ra$ is 1.1, suggesting a weak influence of rotation on the convection. After statistical equilibration the Nusselt number is about 3, the Reynolds number is about 10, and the fraction of the kinetic energy in the axisymmetric flow after three hours of simulated time is 90%. This last value is much higher than for the above cases with $H = 0$.

Figure 9(*a*, *b*) (Plate 4) shows graphical snapshots of our simulation. The striking characteristics of this scenario are the spiral updrafts that extend from the pole to mid-latitude at about a 45° angle. This 'spiral-wave' pattern does not dominate the whole hemisphere. At the same time, part of the hemisphere is dominated by narrow

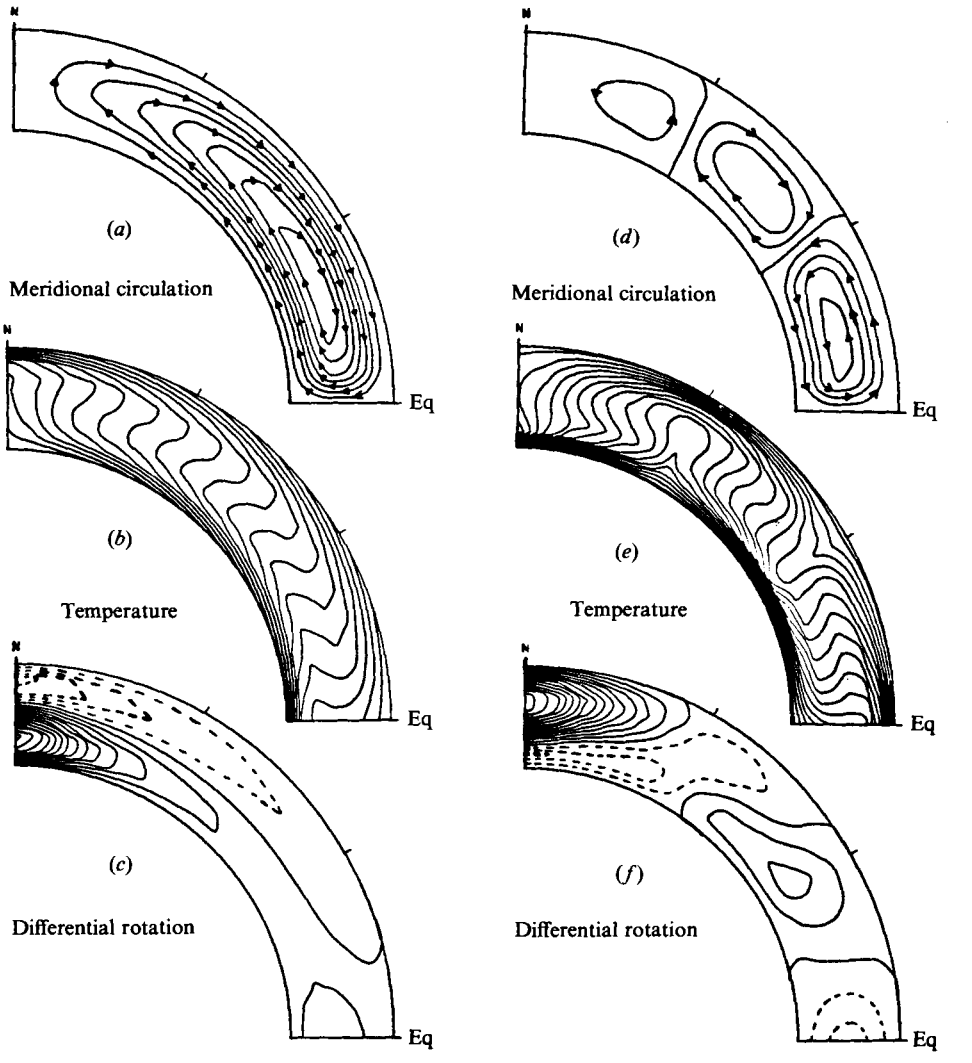

FIGURE 11. Plots of longitudinally averaged quantities obtained from numerical simulations, (*a*)–(*c*) as in figure 9(*a*) for spiral waves, (*d*)–(*f*) as in figure 12(*b*) for banded structures. (*a*) and (*d*) show streamlines of meridional velocity. (*b*) and (*e*) give contours of temperature. (*c*) and (*f*) show contours of relative angular velocity (solid = prograde).

north–south updrafts that extend from the pole to the equator without a significant inclination angle. All features propagate in the prograde direction (i.e. right to left). This simulation qualitatively agrees with the experiment. Indeed for conditions near this Rayleigh number, as well as for higher values, a mixture of spiral waves tilting eastward with latitude and non-inclined north–south cells have been observed and are illustrated in figure 5(*d*,*f*).

In an attempt to understand the maintenance of the computed convective structure we consider the effect of the imposed latitudinal temperature difference on the axisymmetric flow which, as mentioned above, represents 90 % of the total kinetic energy. Since fluid is cooled at the outer boundary and since the pole is hotter than the equator, the fluid flow near the outer boundary is from the pole to the equator. The resulting meridional circulation is illustrated in figure 11(*a*), which shows

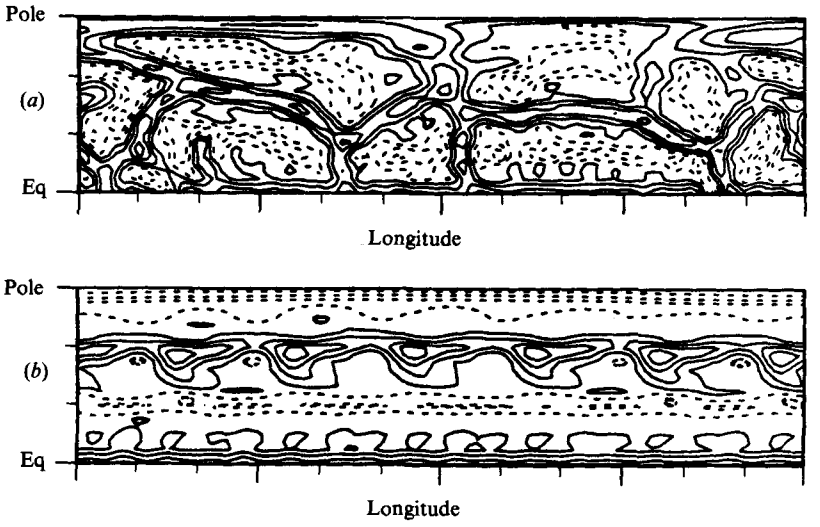

FIGURE 12. Radial velocity at mid-depth on a Mercator projection from the evolving numerical simulation. Both have $Ta = 1.1 \times 10^3$, $Ra = 8.4 \times 10^3$, and $H = 1$. (*a*) after 20 min, (*b*) after 2.5 h. (Solid = outward).

meridional streamlines; figure 11 (*b*) shows the longitudinally averaged meridional temperature profile. The Coriolis forces resulting from the meridional circulation produce a differential rotation (figure 11 *c*) with eastward flow in the equatorial region and near the inner boundary where fluid flows toward the axis of rotation, and westward flow near the outer boundary where fluid flows away from the axis. This strong differential rotation at small radii, increasing poleward, shears out the non-axisymmetric convection into spirals.

4.3. *Soccer balls: slow rotation, $H = 0$*

We now describe a scenario with slow rotation that has the same Rayleigh and Taylor numbers ($Ra = 8.4 \times 10^3$, $Ta = 1.1 \times 10^3$, 48 s rotation period) as in the previous example, but here the north–south temperature gradient is absent ($H = 0$). Figure 5 (*g*) shows a Schlieren photograph of the actual experiment for this scenario. The same convective pattern appears during the first hour of our numerical simulation. Figure 12 (*a*) shows a Mercator projection of our simulated radial component of velocity on a constant-radius surface.

The numerical simulation was continued for 2.5 h even though the spin-up time ($d/(\Omega\nu)^{\frac{1}{2}}$) is only about 0.5 min. Recall that the corresponding laboratory experiment was run for only one hour during the flight. After the first hour, our numerical simulation slowly evolved from the 'soccer-ball' pattern into a more axisymmetric pattern with hot, narrow upflow bands near the equator and near 60° latitude and cool downflow bands near 30° latitude and near the pole. This banded structure is illustrated in figure 11 (*d*), showing streamlines of meridional circulation. This three-celled pattern is preferred in this slow-rotation case because the aspect ratio of the cells, in radius and latitude, is close to unity which is a compromise between the pressure-gradient work required to drive the horizontal flow and the viscous work resulting from the curvature of the flow. A comparison of figure 11 (*d*) with 11 (*e*), a plot of the longitudinally averaged temperature profile, displays the correlation between the radial component of velocity and the fluid temperature. The longitudinal component of velocity also becomes nearly axisymmetric owing to the Coriolis forces

resulting from the meridional flow. That is, a strong retrograde flow (in the rotating frame of reference) develops near the equator owing to fluid moving away from the rotation axis, while a strong prograde (eastward) flow develops near 30° latitude because there fluid moves toward the rotation axis. At high latitude, fluid flows toward the pole near the outer boundary producing an eastward flow (cf. figure 11*d*); near the inner boundary it flows away from the pole producing a westward flow. This is illustrated in figure 11(*f*) with contours of differential rotation. Although Coriolis forces dominate the maintenance of differential rotation, the convergence of the nonlinear Reynolds stress also makes a contribution, especially in the polar region. There the convergence of angular momentum helps to maintain the prograde polar vortex that appears in figure 11(*f*). In addition to this axisymmetric structure, as the flow evolved, a longitudinal wavenumber $m = 2$ pattern developed at high latitude with two large downdraughts on opposite sides of the globe. After about 1.5 h, kinetic energy at high latitude shifted from the $m = 2$ fluctuation to an $m = 6$ dominance (figure 12*b*) while maintaining a fairly axisymmetric banded structure at low latitude. This appears to be the final state.

In addition to this change in the convective structure, a very definite change in the phase propagation of the patterns occurred. During the first 1.5 h of our simulation the phase of the convection pattern propagated in a prograde direction when viewed in the rotating frame of reference. However, when the $m = 6$ mode became dominant at high latitude, it propagated in a retrograde sense. Then, within a few minutes, features at all other latitudes also began propagating in the retrograde sense. This new structure and phase propagation continued for the rest of our simulation.

During this 2.5 h simulation, the total kinetic energy of the fluid remained fairly constant, and the Reynolds number was typically 10. However, the kinetic energy in the axisymmetric flow, i.e. meridional circulation and differential rotation, increased from about 50% of the total kinetic energy near the beginning of the simulation to over 90% at 2.5 h. The thermal-energy spectrum (temperature variance versus longitudinal wavenumber m) during the 'soccer-ball' phase has a maximum in the axisymmetric ($m = 0$) mode with energy per wavenumber dropping almost four orders of magnitude by $m = 31$. The kinetic-energy spectrum has a similar profile. A secondary peak develops at $m = 6$ near the end of the simulation. During our 2.5 h simulation, the Nusselt number remained nearly constant at about 2.69 ± 0.03. This suggests that the different convection modes, which dominated at different times during the simulation, were nearly equally efficient in transporting heat. Such long evolution times are typical in nonlinear systems that have modes with nearly equal growth rates. The identification of the competing modes in this problem is a desirable but complicated exercise beyond the scope of this paper.

4.4. *Triangular waves: rapid rotation, $H \neq 0$*

Finally, we consider a complex situation with rapid rotation, a relatively high Rayleigh number and a large pole-to-equator temperature difference. We set $Ta = 6.1 \times 10^5$ (a 2 s rotation period), $H = 1.38$, and $Ra = 4.2 \times 10^4$. The Nusselt and Reynolds numbers for this scenario are about 4 and 20 respectively. The differential rotation represents about 10% of the total kinetic energy, while the energy in the meridional circulation is about 0.5% of the total. These proportions are higher than those for the rapid rotation, $H = 0$ cases (banana cells), but smaller than those for the slow rotation, $H \neq 0$ cases (spiral waves). The profiles of the differential

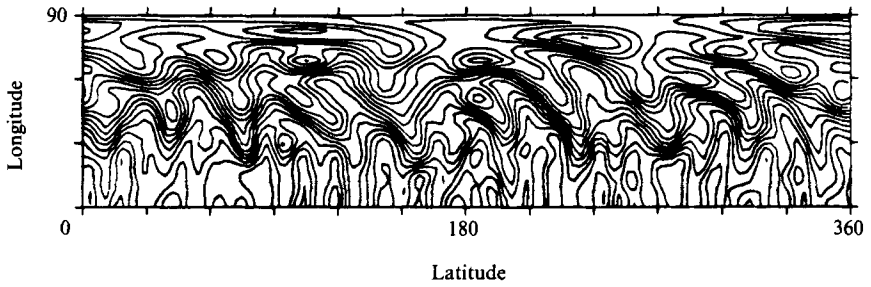

FIGURE 13. Temperature field at mid-depth at one instant in time for $Ta = 6.1 \times 10^5$, $H = 1.38$, $Ra = 4.2 \times 10^4$.

rotation and meridional circulation for this scenario are similar to those of the spiral-wave case shown in figure 11 (a, c).

The striking characteristic of the corresponding experiment is the 'triangular-wave' pattern at mid-latitude (figure 5h). We also see some indication of triangularly shaped ridges at mid-latitude in the temperature field of our numerical simulation (figure 13). These triangular patterns propagate in a retrograde direction along with the features at high latitude, while the features at low latitude propagate in a prograde direction.

Cine films of the radial component of velocity in the simulation clearly show banana cells at low latitude propagating in the prograde direction and a less organized convective pattern at high latitude propagating in the retrograde direction. The maximum phase speed is fairly small compared with the maximum fluid velocity of 0.2 cm/s. Patterns at low latitude tilt in the prograde direction while those at high latitude tilt in the retrograde direction. The interference of these two oppositely tilting patterns at mid-latitude may be responsible for the triangular ridges seen in the temperature field, which is the sum of the non-axisymmetric temperature perturbations corresponding to these radial velocity patterns and an axisymmetric, latitudinally increasing background temperature imposed by the boundary conditions.

5. Summary

We have studied thermal convection in a rotating hemispherical shell by comparing our laboratory results with three-dimensional numerical simulations. We have found nice qualitative and encouraging quantitative agreement between our simulations and laboratory experiments over a wide range of rotation rates, gravities and thermal boundary conditions. One can compare, for example, the computationally derived thermal-energy spectra in figure 14 with the corresponding experimental cases in figure 7. For the 'banana-cell' convection the major peak at about $m = 15$ is found in both systems (see figures 14a, 7a). For the 'triangular-wave' case, the non-axisymmetric energy peaks at $m = 9$ and 12, and 13 respectively (figures 14c, 7c). Only for the 'spiral waves' do the two measurements significantly disagree, with the numerical peak being at $m = 8$ compared with $m = 14$ for the experiment (figures 14b, 7b). The experiments show that in this case, small changes in the Rayleigh number can cause large shifts in the peaks of the power spectra.

We have found that when both the rotation rate and thermal driving are small, the majority of the kinetic energy is in the axisymmetric flow. The non-axisymmetric flow tends to be characterized by narrow updraughts and broad downdraughts. In

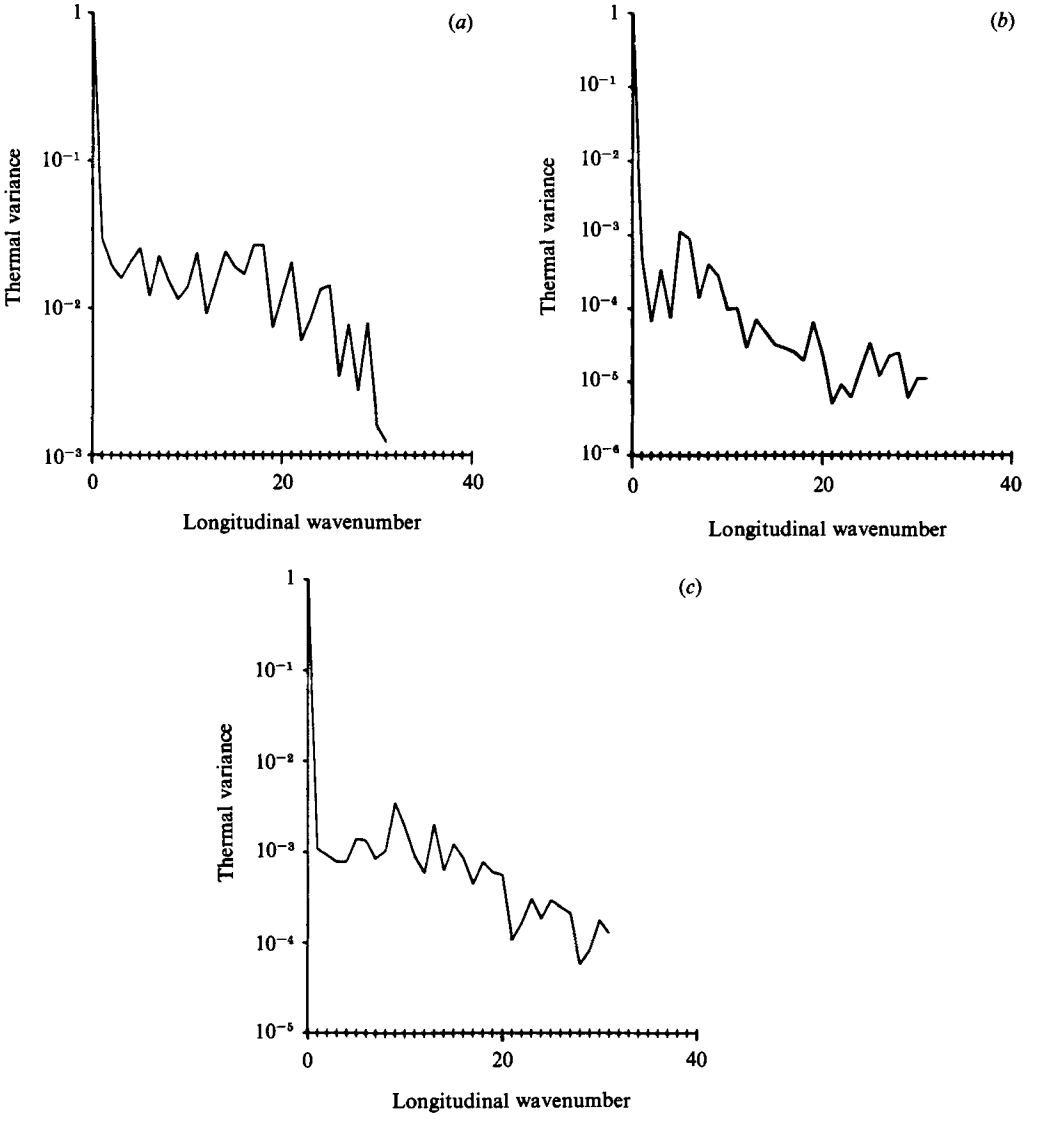

FIGURE 14. Thermal-variance spectra obtained from numerical simulations for (*a*) $Ta = 6.1 \times 10^5$, $H = 0$, $Ra = 7.9 \times 10^4$ (banana cells); (*b*) $Ta = 1.1 \times 10^3$, $H = 1.0$, $Ra = 8.4 \times 10^3$ (spiral waves); (*c*) $Ta = 6.1 \times 10^5$, $H = 1.38$, $Ra = 4.2 \times 10^4$ (triangular waves).

addition, when the boundary temperature did not vary with latitude, the axisymmetric flow was banded in latitude and the non-axisymmetric structure in the computations slowly evolved from a polygonal tiling pattern ('soccer ball') to a strong meridional cell with superimposed travelling waves. However, the total heat flux remained essentially constant during this evolution. On the other hand, when a pole–equator temperature difference was imposed on the boundaries, a strong single-celled meridional circulation developed which maintained a differential rotation with an eastward jet in the equatorial region. The associated non-axisymmetric flow was characterized by narrow updraughts sheared out into spirals by the zonal flow.

In the high-rotation cases, most of the kinetic energy is in the non-axisymmetric

flow. 'Banana cells' dominate at low latitude as suggested by the Taylor–Proudman theorem. When a pole-to-equator temperature difference was imposed on the boundaries, 'triangular' patterns developed in the temperature field at mid-latitude. Our computations suggest that they may be due to the interference of the prograde-propagating convective patterns at the low latitude and the retrograde-propagating patterns at high latitude. With the detailed information available from our numerical simulations we shall attempt to understand the basic physics responsible for some of the simpler convective structures that were observed in the Spacelab experiment. One project is to determine the linear eigenfunctions for unstable modes of the non-conductive axisymmetric basic states. Another is to investigate the role of the r^{-5} gravity in breaking planform degeneracies.

It is discouraging that as the convective structure and evolution become very complicated, the time-dependent nonlinear interaction of thousands of spectral modes in our numerical simulations becomes as difficult to understand as the actual experiment. It is gratifying, however, to see that the basic entities called Taylor columns, brought to light some 65 years ago in the fundamental experiments of G. I. Taylor (1921), appear again as organizing centres for convection in rotating spherical shells with central buoyancy forces over a wide range of external conditions. Our experiments have shown how these disturbances are modified when mid-latitude modes arise as the Rayleigh number is increased, or as the meridional circulation becomes large when an equator-to-pole temperature difference is imposed. They have illustrated the myriad and striking forms of fluid motion that can apparently occur in geometrically simple models of global convection with rotation and radial gravity. It is hoped that our results will in a small way inspire further exploration in this intriguing field.

Many people have been involved with this project over the years, and without their assistance and encouragement it surely would not have reached fruition. We would especially like to thank Dr Fred Leslie of the Marshall Space Flight Center, one of our co-investigators, for his untiring work with an occasionally cantankerous instrument that in the end performed almost flawlessly. The other members of the co-investigator group, Dr George Fichtl and Dr William Fowlis of MSFC, and Dr Peter Gilman of the National Center for Atmospheric Research, have provided continuing technical and theoretical guidance, and insights into the underlying dynamics. We thank Robert Malone for recent helpful discussions concerning numerical modelling. Anil Deane and Neal Hurlburt from the University of Colorado also participated in mission operations, and they with Bill Merryfield have assisted with the digital processing (still continuing) of the photographic data. Thanks are also due Ray Kroger, and his colleagues at Aerojet Electrosystems, who built the flight hardware. We are most grateful for financial support from the National Aeronautics and Space Administration through contract NAS-8-31958 to the University of Colorado.

Appendix. The numerical procedure

We shall here outline the semi-implicit, spectral representations that we employ in our nonlinear simulations of the three-dimensional convection. Within the Boussinesq approximation for an incompressible fluid, the density perturbation is not a function of the pressure perturbation. Therefore, we can remove the pressure from the system of equations by taking the curl of (16) and use the resulting vorticity

($\nabla \times \boldsymbol{v}$) equation. Equation (15) allows us to write the velocity in terms of its poloidal W and toroidal Z scalar functions. In addition, we need the poloidal part, ζ, of vorticity. Then W, Z, ζ, and T are expanded in spherical harmonics Y_l^m with complex coefficients that are functions of radius and time. As a result, the radial, colatitudinal (Θ), and longitudinal components of velocity are

$$v_r = \frac{1}{r^2} \sum_{l,m} l(l+1)\, W_l^m\, Y_l^m, \tag{A 1}$$

$$v_\Theta = \frac{1}{r \sin\Theta} \sum_{l,m} \left(\frac{\partial W_l^m}{\partial r} \sin\Theta \frac{\partial Y_l^m}{\partial \Theta} + Z_l^m \frac{\partial Y_l^m}{\partial \phi} \right), \tag{A 2}$$

$$v_\phi = \frac{1}{r \sin\Theta} \sum_{l,m} \left(\frac{\partial W_l^m}{\partial r} \frac{\partial Y_l^m}{\partial \phi} - Z_l^m \sin\Theta \frac{\partial Y_l^m}{\partial \Theta} \right), \tag{A 3}$$

the radial component of vorticity is

$$(\nabla \times \boldsymbol{v})_r = \frac{1}{r^2} \sum_{l,m} l(l+1)\, Z_l^m\, Y_l^m, \tag{A 4}$$

the radial component of the curl of vorticity is

$$(\nabla \times \nabla \times \boldsymbol{v})_r = \frac{1}{r^2} \sum_{l,m} l(l+1)\, \zeta_l^m\, Y_l^m, \tag{A 5}$$

where

$$\zeta_l^m = \frac{l(l+1)}{r^2} W_l^m - \frac{\partial^2 W_l^m}{\partial r^2}, \tag{A 6}$$

and the temperature perturbation is

$$T = \sum_{l,m} T_l^m\, Y_l^m. \tag{A 7}$$

As discussed in Glatzmaier (1983), the spherical-harmonic coefficients are expanded in Chebyshev polynomials to describe their radial dependence.

A prognostic equation for Z_l^m is obtained from the radial component of the curl of (16). The linear terms in this equation involve $W_{l\pm1}^m$, $\partial W_{l\pm1}^m/\partial r$, Z_l^m, and $\partial^2 Z_l^m/\partial r^2$. The radial component of the curl of the curl of (16) provides a prognostic equation for ζ_l^m. The linear terms in this equation involve T_l^m, $Z_{l\pm1}^m$, $\partial Z_{l\pm1}^m/\partial r$, ζ_l^m, and $\partial^2 \zeta_l^m/\partial r^2$. The diagnostic equation (A 6) is solved for W_l^m. Finally, a prognostic equation for T_l^m is obtained directly from (17).

This system of equations is eighth-order in space and third-order in time. Small, random perturbations in the temperature field and a zero velocity field relative to the rotating frame of reference provide the initial conditions. The impermeable and non-slip boundary conditions require W_l^m, $\partial W_l^m/\partial r$, and Z_l^m to vanish at the inner and outer boundaries for all l and m. If a zero latitudinal temperature gradient is specified on the boundaries, all T_l^m vanish there. If, however, a non-zero equator–pole temperature difference is specified, all T_l^m, except T_0^0 and T_2^0, vanish on the boundaries. At the inner boundary

$$T_0^0 = \tfrac{2}{3}(4\pi)^{\frac{1}{2}} \left(\frac{T_{ie} - T_{ip}}{T_{ip} - T_{op}} \right), \tag{A 8}$$

$$T_2^0 = -\tfrac{2}{3}(\tfrac{4}{5}\pi)^{\frac{1}{2}} \left(\frac{T_{ie} - T_{ip}}{T_{ip} - T_{op}} \right), \tag{A 9}$$

and at the outer boundary

$$T_0^0 = \tfrac{2}{3}(4\pi)^{\frac{1}{2}} \left(\frac{T_{oe} - T_{op}}{T_{ip} - T_{op}} \right), \tag{A 10}$$

$$T_2^0 = -\tfrac{2}{3}(\tfrac{4}{5}\pi)^{\frac{1}{2}} \left(\frac{T_{oe} - T_{op}}{T_{ip} - T_{op}} \right), \tag{A 11}$$

where the subscripts o, i, e, and p on the specified boundary temperature stand for outer, inner, equator and pole respectively. This provides smooth, monotonic, axisymmetric, latitudinal temperature profiles on the boundaries.

In addition, since we are modelling a hemisphere with an impermeable equatorial plane, we force symmetry with respect to the equator by making ζ_l^m, W_l^m and T_l^m vanish for odd $(l+m)$ and Z_l^m vanish for even $(l+m)$. As a result, the colatitudinal component of velocity vanishes at the equator; however, the radial and longitudinal components do not. Since the equatorial plane is non-slip in the actual experiment, the model-simulated velocity profiles at the equatorial plane differ somewhat from those observed in the experiment. However, the difference appears to be insignificant a short distance from the equatorial plane.

The prognostic equations for ζ_l^m, Z_l^m and T_l^m are integrated in time with a second-order, semi-implicit scheme via Chebyshev collocation. All spatial derivatives are computed analytically in spectral space; and all nonlinear terms are computed in physical space. The longitudinal and radial transformations between spectral and physical space, which are required at every timestep, are done via fast Fourier transforms; the latitudinal transformations are done via Gaussian quadratures. The method is described in Glatzmaier (1983); however, we have made the following modification. The prognostic equation for ζ_l^m and the diagnostic equation (A 6) for W_l^m, both second-order in space, are solved simultaneously with a matrix equation for each l and m. The four boundary conditions required for this subsystem are the two conditions on W_l^m and the two conditions on $\partial W_l^m/\partial r$; no boundary condition is applied on ζ_l^m.

Finally, we should comment on the spatial and temporal resolutions. In physical space, there are 96 longitudinal mesh points (spanning 360°) times 24 latitudinal mesh points (pole to equator) times 17 radial mesh points (inner to outer boundary). In spectral space, the spherical harmonics are truncated according to $0 \leqslant |m| \leqslant l \leqslant 31$, which results in alias-free horizontal transformations. The Chebyshev polynomials are truncated at wavenumber 16. Our temporal resolution is dictated by the Courant condition; in terms of the physical variables in the laboratory experiment, the computational timestep is typically between 0.1 and 0.5 s. More than 3 h have been simulated for some scenarios, which corresponds to several hundred rotations. For Rayleigh numbers of order 10^4, the CPU time required on a Cray XMP supercomputer is comparable with the actual experimental time that is simulated. For higher values, the increased spatial resolution that is required rapidly drives up the CPU time to the point that numerical simulation becomes impractical.

REFERENCES

Atten, P. & LaCroix, J. C. 1979 Nonlinear hydrodynamic stability of liquids subject to unipolar injection. *J. Méc.* **18**, 469–510.

Busse, F. H. 1970 Thermal instabilities in rotating systems. *J. Fluid Mech.* **44**, 441–460.

Busse, F. H. 1973 Differential rotation in stellar convection zones II. *Astron. Astrophys.* **28**, 27–37.

Busse, F. H. 1983 A model of mean zonal flows in the major planets. *Geophys. Astrophys. Fluid Dyn.* **23**, 153–174.

Busse, F. H. & Carrigan, C. R. 1976 Laboratory simulation of thermal convection in rotating planets and stars. *Science* **191**, 81–83.

Busse, F. H. & Cuong, P. G. 1977 Convection in rapidly rotating spherical fluid shells. *Geophys. Astrophys. Fluid Dyn.* **8**, 17–41.

CARRIGAN, C. R. & BUSSE, F. H. 1983 An experimental and theoretical investigation of the onset of convection in rotating spherical shells. *J. Fluid Mech.* **126**, 287–305.

CHANDRA, B. & SMYLIE, D. E. 1972 A laboratory model of thermal convection under a central force field. *Geophys. Fluid Dyn.* **3**, 211–224.

CHARNEY, J. G. 1947 The dynamics of long waves in a baroclinic westerly current. *J. Met.* **4**, 135–163.

CHARNEY, J. G. & DRAZIN, P. G. 1961 Propagation of planetary scale disturbances from the lower into the upper atmosphere. *J. Geophys. Res.* **66**, 83–109.

DURNEY, B. R. 1970 Nonaxisymmetric convection in a rotating spherical shell. *Astrophys. J.* **161**, 1115–1127.

FINLAYSON, B. A. 1970 Convective instability of ferromagnetic fluids. *J. Fluid Mech.* **40**, 753–767.

GILMAN, P. A. 1973 Convection in a rotating annulus uniformly heated from below. Part 2. Nonlinear results. *J. Fluid Mech.* **57**, 381–400.

GILMAN, P. A. 1975 Linear simulations of Boussinesq convection in a deep rotating spherical shell. *J. Atmos. Sci.* **32**, 1331–1352.

GILMAN, P. A. 1977 Nonlinear dynamics of Boussinesq convection in a deep rotating spherical shell. I. *Geophys. Astrophys. Fluid Dyn.* **8**, 93–135.

GILMAN, P. A. 1978 Nonlinear dynamics of Boussinesq convection in a deep rotating spherical shell. III. Effects of velocity boundary conditions. *Geophys. Astrophys. Fluid Dyn.* **11**, 181–203.

GILMAN, P. A. 1986 The solar dynamo: observations and theories of solar convection, global circulations and magnetic fields. *Physics of the Sun* (ed. P. A. Sturrock), vol. 1, chap. 5, pp. 95–160. Reidel.

GLATZMAIER, G. A. 1983 Numerical simulations of stellar convective dynamos. I. The model and method. *J. Comp. Phys.* **55**, 461–484.

GLATZMAIER, G. A. 1985 Numerical simulations of stellar convective dynamos. II. Field propagation in the convection zone. *Astrophys. J.* **291**, 300–307.

GLATZMAIER, G. A. & GILMAN, P. A. 1981 Compressible convection in a rotating spherical shell. II. A linear anelastic model. *Astrophys. J. Suppl.* **45**, 351–380.

HART, J. E. 1976 Studies of Earth simulation experiments. *NASA Rep.* CR-2753, 66 pp.

HART, J. E. & TOOMRE, J. 1977 Geophysical fluid dynamics with dielectric polarization forces. *Rep.* 2, NASA Contract NAS-8-31958, 65 pp. (available from JEH or JT).

HART, J. E., TOOMRE, J., DEANE, A. E., HURLBURT, N. E., GLATZMAIER, G. A., FICHTL, G. H., LESLIE, F., FOWLIS, W. W. & GILMAN, P. A. 1986 Laboratory experiments on planetary and stellar convection performed on Spacelab 3. *Science* (to appear September 1986).

INGERSOL, A. P. 1976 Pioneer 10 and 11 observations and the dynamics of Jupiter's atmosphere. *Icarus* **29**, 245–251.

INGERSOL, A. P., REVERCOMB, H. E., SROMOVSKY, L. A., KRAUSS, J. R., SANTEK, D. A., SOVMI, V. E., COLLINS, S. A. & ARIS, C. C. 1980 Interaction of eddies and mean zonal flow on Jupiter as inferred from Voyager 1 and Voyager 2 images. *J. Geophys. Res.* **86**, 8733–8743.

MARKIEWICZ, W. J. & ALDRIDGE, K. D. 1982 Dielectrophoretic thermal instability in a spherical shell of fluid. *Geophys. Astrophys. Fluid Dyn.* **21**, 225–236.

MELCHER, J. R. & TAYLOR, G. I. 1969 Electrohydrodynamics: A review of the role of interfacial shear stress. *Ann. Rev. Fluid Mech.* **1**, 111–146.

MOFFATT, H. K. 1978 *Magnetic Field Generation in Electrically Conducting Fluids.* Cambridge University Press.

OSTRACH, S. 1982 Low-gravity fluid flows. *Ann. Rev. Fluid Mech.* **14**, 313–345.

PANOFSKY, W. H. K. & PHILLIPS, M. 1955 *Classical Electricity and Magnetism.* Addison-Wesley.

PARKER, E. N. 1979 *Cosmical Magnetic Fields: Their Origin and Activity.* Oxford University Press.

PROUDMAN, J. 1916 On the motion of solids in a liquid possessing vorticity. *Proc. R. Soc. Lond.* A **92**, 408–424.

ROBERTS, P. H. 1969 Electrohydrodynamic convection. *Q. J. Mech. Appl. Maths* **22**, 211–220.

SMYLIE, D. E. 1966 Thermal convection in dielectric liquids and modelling in geophysical fluid dynamics. *Earth Planet. Sci. Lett.* **1**, 339–340.

STRATTON, J. A. 1941 *Electromagnetic Theory*. McGraw-Hill.

TAYLOR, G. I. 1921 Experiments with rotating fluids. *Proc. R. Soc. Lond.* A **100**, 114–121.

TURNBULL, R. J. 1971 Instability of a thermal boundary layer in a constant electric field. *J. Fluid Mech.* **47**, 231–239.

TURNBULL, R. J. & MELCHER, J. R. 1969 Electrohydrodynamic Rayleigh–Taylor bulk instability. *Phys. Fluids* **12**, 1160–1166.

WORRAKER, W. J. & RICHARDSON, A. T. 1981 A nonlinear electrohydrodynamic stability analysis of a thermally stabilized plane layer of dielectric liquid. *J. Fluid Mech.* **109**, 217–237.